ACS SENSORS

Article

Cite This: ACS Sens. 2019, 4, 3175−3185

pubs.acs.org/acssensors

Fully Passive Flexible Wireless Neural Recorder for the Acquisition of Neuropotentials from a Rat Model

Shiyi Liu,*[,†] Carolina Moncion,[‡] Jianwei Zhang,[†] Lakshmini Balachandar,[‡] Dzifa Kwaku,[†] Jorge J. Riera,[‡] John L. Volakis,[‡] and Junseok Chae[†]

[†]School of Electrical, Computer and Energy Engineering, Arizona State University, Tempe, Arizona 85287, United States

[‡]NMD Laboratory, Department of Biomedical Engineering, Florida International University, Miami, Florida 33174, United States

Supporting Information

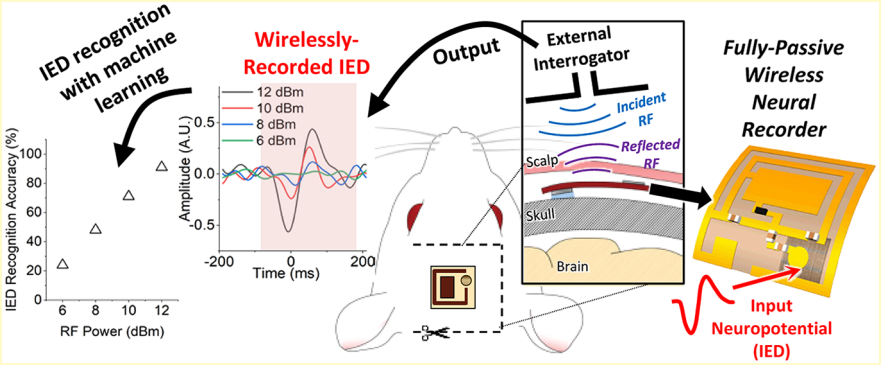

ABSTRACT: Wireless implantable neural interfaces can record high-resolution neuropotentials without constraining patient movement. Existing wireless systems often require intracranial wires to connect implanted electrodes to an external head stage or/and deploy an application-specific integrated circuit (ASIC), which is battery-powered or externally power-transferred, raising safety concerns such as infection, electronics failure, or heat-induced tissue damage. This work presents a biocompatible, flexible, implantable neural recorder capable of wireless acquisition of neuropotentials without wires, batteries, energy harvesting units, or active electronics. The recorder, fabricated on a thin polyimide substrate, features a small footprint of 9 mm × 8 mm × 0.3 mm and is composed of passive electronic components. The absence of active electronics on the device leads to near zero power consumption, inherently avoiding the catastrophic failure of active electronics. We performed both in vitro validation in a tissue-simulating phantom and in vivo validation in an epileptic rat. The fully passive wireless recorder was implanted under rat scalp to measure neuropotentials from its contact electrodes. The implanted wireless recorder demonstrated its capability to capture low voltage neuropotentials, including somatosensory evoked potentials (SSEPs), and interictal epileptiform discharges (IEDs). Wirelessly recorded SSEP and IED signals were directly compared to those from wired electrodes to demonstrate the efficacy of the wireless data. In addition, a convoluted neural network-based machine learning algorithm successfully achieved IED signal recognition accuracy as high as 100 and 91% in wired and wireless IED data, respectively. These results strongly support the fully passive wireless neural recorder's capability to measure neuropotentials as low as tens of microvolts. With further improvement, the recorder system presented in this work may find wide applications in future brain machine interface systems.

KEYWORDS: *neural recorder, implantable, wireless, flexible, fully passive*

Neuropotentials provide invaluable clinical and scientific information to help us understand brain functionality and diagnose neurological diseases.[1−3] Brain machine interface (BMI) records and transmits neuropotentials to an external apparatus for analysis and study. The low frequency (<500 Hz) components of the neuropotentials recorded by the BMI can generally be classified into three categories: electroencephalogram (EEG), electrocorticogram (ECoG), and stereo-electroencephalography (sEEG), corresponding to signals measured on scalp, on the cortical surface, and within cortical tissue, respectively.[4] Among them, EEG is the safest and most widely used clinical tool. However, the recorded EEG signal is a summation of neural activities over a relatively large area—a few square centimeters of the cortex.[1,4] The poor spatial resolution of EEG often results in diagnostic failure to recognize interictal epileptiform discharge (IED) in patients with seizure disorders.[1] ECoG or sEEG offers much improved temporal and spatial resolution because the electrodes are directly implanted on or inside the cortex.[4,5] However, the surgical procedure of ECoG/sEEG is invasive, and long wire

Received: August 5, 2019
Accepted: October 31, 2019
Published: October 31, 2019

DOI: 10.1021/acssensors.9b01491
ACS Sens. 2019, 4, 3175−3185

bundles are needed to connect implanted electrodes to external instruments. Thus, recording of ECoG/sEEG is generally conducted during brain surgery for only a short period of time (intra-operative)[6,7] or during a few weeks in between two consecutive surgical procedures (extra-operative). In either case, the cabled ECoG/sEEG electrodes have become the major cause of a series of complications, including bleeding,[8−10] cerebrospinal fluid (CSF) leakage,[9] urinary tract infection,[8] and osteomyelitis.[10] In addition, the tethered recording protocol greatly constrains the free movement of patients, causing discomfort or disfiguration.[11,12]

To overcome the limitation associated with wires and cables, extensive studies have been conducted in the field of developing completely wireless, implantable ECoG/sEEG recording systems.[12−17] In these studies, one common practice is to insert a microelectrode array (MEA), such as the Utah,[14−16] Michigan,[18] or μECoG[17,19] array, onto the cortex surface, while placing the remaining system outside the skull in the form of the head stage[12,14,16,20,21] or subcutaneous microsystem.[15] Connections between the implanted electrodes and the external system are accomplished using a bundle of cables penetrating through the skull. This separation of the MEA and external system largely alleviates the stringent design requirements imposed on the wireless system, such as size and power consumptions.[22] Indeed, with this approach, many researchers have reported successful wireless neuropotential acquisition of hundreds or thousands of channels from freely moving animals.[12] However, the intracranial wiring configuration also gives rise to numerous challenges and issues. A major concern is the high failure rate. Barrese et al.[23] examined the long-term functionality of 78 MEA head stages mounted on primates. It was discovered that 48% of the arrays completely lose functionality within one year because of mechanical failures associated with transcranial cables. Notably, the protrusion of the head stage from the skin makes them particularly susceptible to external damage, causing the breakage of intracranial wire bundles, removal of implanted MEA, or even cortical injury. Besides this high failure rate, other potential issues include the risk of infection at the surgical wound[24] and the negative impact of the head stage on the patient's cosmetic appearance.

The problems mentioned above can be effectively solved if the entire wireless system, rather than only part of it, is implanted onto the cortical surface to enable complete closure of surgical wound. However, developing such a fully implanted wireless system faces tremendous technical challenges because of the restriction in size, power consumption, biocompatibility, and long-term reliability.[17,25,26] Batteries should also be avoided because of their limited lifetime and hazardous content.[27] In the past years, researchers have been resorting to the ultralow power consumption integrated circuit (IC) technology to overcome these challenges.[16,28,29] Muller et al.[17] developed a 64-channel fully implantable wireless micro-ECoG array which incorporated a specially designed low power IC with microfabricated parylene electrodes. The IC, powered by an external inductive coil, was very promising and exhibited a low power consumption of 225 μW and a footprint of 2.4 mm × 2.4 mm. Another wireless ECoG system was proposed by Mestais et al.[30] Although this system was intended for placement under the skull, it was only validated in air with intracranial cables connected to a commercial cortical array, greatly diminishing the efficacy of the study. The system's large footprint of 50 mm in diameter and 12.54 mm in height, high power consumption of 350 mW, and rigid printed circuit board (PCB) structure may result in safety issues for long-term implantation. In short, existing wireless implantable systems based on the active integrated IC technology have not been effective in addressing the aforementioned challenges, partly because of their rigidity, high power consumption, and lack of potential long-term reliability.

This article reports a biocompatible, flexible, fully passive wireless neural recorder, capable of measuring neuropotentials from the brain by receiving, modulating, and backscattering radio frequency (RF) microwave generated from an external interrogator. Different from the previous systems based on the active IC technology, the proposed wireless recorder is composed entirely of passive components. The wireless neuropotential acquisition using the RF backscattering mechanism allows the recorder to achieve near zero power consumption. Fabricated on a thin flexible polyimide substrate, the proposed wireless recorder features a footprint of 9 mm × 8 mm × 0.3 mm. Our previously reported silicon-based fully passive wireless recorder demonstrated a minimum detectable voltage of 500 μV_{pp}, when recording from frog sciatic nerve in vivo.[31] Another previous work reported in vivo validation of the fully passive wireless system using somatosensory evoked potentials (SSEPs).[32] This work was performed by wiring the electrode inside the scalp to the external wireless system. In this article, we evaluate the biocompatible and flexible recorder in a practical implanted environment, using both an invitro tissue-simulating phantom model and an in vivo epileptic rat model. The fully passive wireless neurorecorder is first embedded inside a tissue-simulating phantom to characterize its functionality, prior to being implanted subcutaneously on the skull of an epileptic rat to measure SSEPs and IEDs. The results obtained by this work may provide valuable insights for future development of fully passive wireless neural recording techniques.

MATERIALS AND METHODS

Animal Preparation. All the in vivo experimental procedures were approved by and carried out in compliance with the Institutional Animal Care and Use Committee (IACUC) at Florida International University (approval no. 17-042). Wistar rats with weight >460 g were housed in standard cages and kept under a 12−12 h light−dark cycle. They were allowed continuous free access to food and water. Upon arrival from Charles River Laboratories (Wilmington, MA), they were allowed to acclimate for 1 week before initiating any of the recordings. To prepare for the experiments, the rats were anesthetized with isoflurane (5% for induction, 1.5−2.5% during surgical procedure, 1 L/min O_2, 14.7 PSI). Rats were fixed in stereotaxy (Narishige, Japan) to implant the device and during the recording. Prior to starting neural recordings, the rats were sedated with a mixture of dexmedetomidine hydrochloride (Dexdomitor, 0.25 mg/kg, i.p.) and kept at low dose isoflurane (0.5%, 1 L/min O_2, 14.7 PSI). Body temperature was monitored throughout the experiment and maintained at approximately 36 °C using a heating pad. The respiration rate was maintained between 50 and 60 breaths per minute while under isoflurane sedation.

In Vivo Neuropotential Acquisition. *Wireless Recorder Implantation.* The schematics of the experimental configuration for in vivo SSEP and IED recordings are shown in Figures 4A and 5A, respectively. The wired and wireless recordings were performed in sequence for SSEP recording (Figure 4A), whereas they were conducted concurrently for IED recording (Figure 5A). Details of the two protocols are provided in the Discussion section. In both cases, an incision of approximately 20 mm × 20 mm (dashed line in Figures 4A and 5A) was made. The wireless recorder was placed on the skull, and conductive paste was used to fix the recording electrode

DOI: 10.1021/acssensors.9b01491
ACS Sens. 2019, 4, 3175−3185

over the left S1HL (primary somatosensory cortex, hind limb region) area of the brain.[33] The rationale for selecting this region will be detailed in Discussion section. The wireless recorder as a whole was fixed to the skull with dental cement. Following this, the skin was placed over the implant and the incision was closed with biocompatible glue. The wired system used a stainless steel needle as the recording electrode. In SSEP recording, the needle electrode was inserted subcutaneously at the very proximity of the location where the wireless recording electrode was located (not shown in Figure 4A). In IED recording, the needle electrode was inserted subcutaneously near the wireless recording electrode (the distance between them is less than 2 mm, Figure 5A). The reference electrodes of the recorder and the wired system were inserted subcutaneously over the contralateral (right) hemisphere of the rat. A robotic arm was also used to hold the external antenna in place, approximately 5 mm over the skin to establish wireless communication with the implanted recorder. An electrocardiogram (ECG) recording was used to calibrate the entire system as ECG generates significantly larger amplitude signals than target neuropotentials. The detailed procedure of calibration using ECG is described in the Supporting Information (Figure S5).

SSEP Signal Recording. An established protocol was used to induce neural activation in the S1HL region of the brain.[32] Specifically, two needle stimulation electrodes were inserted subcutaneously in the rat's right hind paw to deliver electrical pulses (3 Hz, 2.5 mA, 0.5 ms duration, AM System model 2100) and induce repetitive neural activation in the S1HL.[34,35] Given the small area of S1HL, it is difficult to perform simultaneous wired and wireless recordings of SSEPs, and for this reason, the recordings were performed sequentially.[32] Three different RF power levels of 11, 9, and 7 dBm were used. Each of these recordings, along with the wired recording, had duration of approximately 10 min and was digitized at a 2 kHz sampling rate.

IED Signal Recording. The pilocarpine model was used to induce temporal lobe epilepsy in rats of approximately 4 weeks of age, using a procedure similar to that carried out previously in ref 36 and 37. Upon reaching a state of spontaneously recurring seizures, one of the subject rats was used for the in vivo experiments. To explore the effect of different RF power levels on the wireless recorder, we swept the RF power from 12 to 6 dBm at a 2 dBm step. At each power level, wired and wireless recordings were continuously performed for 10 min at 2 kHz sampling rate.

Neuropotential Signal Processing. *SSEP Signal Processing.* We followed the previous method of SSEP signal processing.[32] The wired and wireless signals were first band-pass filtered from 4 to 80 Hz and then notch filtered between 35 and 45 Hz. The filtered signals were then segmented from −50 to 250 ms referenced to the onset of the recorded stimulation pulse. The SSEPs were then obtained by averaging the neuropotential segments using MATLAB-based EEGLab software.

IED Signal Processing. The raw data were first band-pass filtered across 1−125 Hz to remove unwanted noise. The wireless data were further filtered to remove breathing artifact. The IEDs in the wired data were identified and labeled, and those in the wireless data were synchronized with the labeled IEDs. For each labeled IED, we marked the time of the negative peak as 0 ms and sliced the data into 600 ms segments (from 300 ms prepeak to 300 ms postpeak).

IED Recognition via the Machine Learning Algorithm. We adopted a machine learning algorithm to further evaluate the performance of the fully passive wireless recorder. Studies have shown that the signal quality of the data set has significant impact on accuracy.[38,39] Hence, a supervised machine learning algorithm was used to analyze the IED signal identification accuracy in wired and wireless data as a function of RF power from 6 to 12 dBm.

Training Data Set Preparation. The training data set was composed of sliced segments of labeled IEDs and noises. Each segment contains 400 points, and the labeled IED segments were sliced from −85 to 115 ms as referred to the negative peak of the IED spike. The segments were then shifted with a gap of 10 points for 10 times to generate 10 training slices. The total training data set included 1540 wired IED slices, 468 wired noise slices, 110 wireless IED slices at 12 dBm, and 468 wireless noise slices. All the slices were labeled with 0—noise and 1—signal.

Model Configuration and Training. We adopted a simple yet robust machine learning model, where the 1st to 2nd and 3rd to 5th layers were convolutional neural networks and fully connected dense layers, respectively. The model was constructed and trained by Keras with TensorFlow backend. The training epochs were 100.

Recognition Process. A recognition scanning window, containing 400 data points, was created and scanned along each testing data set at an interval of 20 data points. Notably, the data inside the window were fed to the trained model to obtain the recognition estimate (0 or 1). At every step of scanning, the recognition values were added together and stored in a recognition array. After scanning, IEDs were identified from the recognition array to extract several parameters, such as signal energy, recognition value, and signal length to determine IEDs.

RESULTS AND DISCUSSION

Fully Passive Wireless Neural Recorder. Figure 1A illustrates the overall schematic of the fully passive wireless neural recording system, which incorporates two subsystems: a fully passive flexible neural recorder to be implanted and an external interrogator to wirelessly communicate with the implanted recorder using RF electromagnetic (EM) waves.[26,31,32,40−45] The implantable recorder is composed entirely of passive components: a single-layer planar antenna, a backside electrode, three capacitors, an inductor, and a varactor diode.

Figure 1C shows the simplified operation of the system. The external interrogator first generates and transmits a 2.32 GHz RF carrier signal, denoted as f_0, to the implanted recorder. At this RF, capacitors C_1 and C_2 are equivalent to short circuits, resulting in only the RF carrier (f_0) exciting the varactor diode. The Inductor L_1 serves as an RF choke to isolate the neuropotentials V_m from the RF signal f_0. For low frequency neuropotentials (<1000 Hz, denoted as f_m), C_1 and C_2 are open circuits while L_1 becomes the short circuit, allowing neuropotentials (f_m) to directly reach the varactor diode. Hence, both the low frequency neuropotentials (f_m) and the high frequency RF carrier (f_0) appear at the varactor diode, enabling mixing of the two signals (see the Supporting Information for details). Many nonlinear harmonic components, including the third-order mixing product $2f_0 \pm f_m$, are backscattered from the planar antenna to the external interrogator to extract the target neuropotentials (f_m). The third-order harmonic component is chosen over others as the signal-to-noise ratio (SNR) of third-order is higher than others.[31,45] The capacitor C_3 functions as a dc block to protect the neuro cells from the dc component from the varactor. All the values of passive components are listed in the Supporting Information (Table S1).

The fully passive wireless neural recorder was fabricated on a 90 μm-thick polyimide substrate using a standard flexible PCB process. Detailed fabrication and assembling steps are provided in the Supporting Information (Figure S1). Figure 1B shows photographs of the fabricated fully passive flexible wireless neural recorder prototype, highlighting a biocompatible, flexible, and small footprint of $9 \times 8 \times 0.3$ mm^3.

The fully passive wireless recorder operates on the basis of the RF backscattering method, and thus, no amplifier exists on the implant capable of amplifying the signal strength before/after the varactor's mixing. Consequently, the sensitivity of the recorder depends heavily on design and optimization of the

DOI: 10.1021/acssensors.9b01491
ACS Sens. 2019, 4, 3175−3185

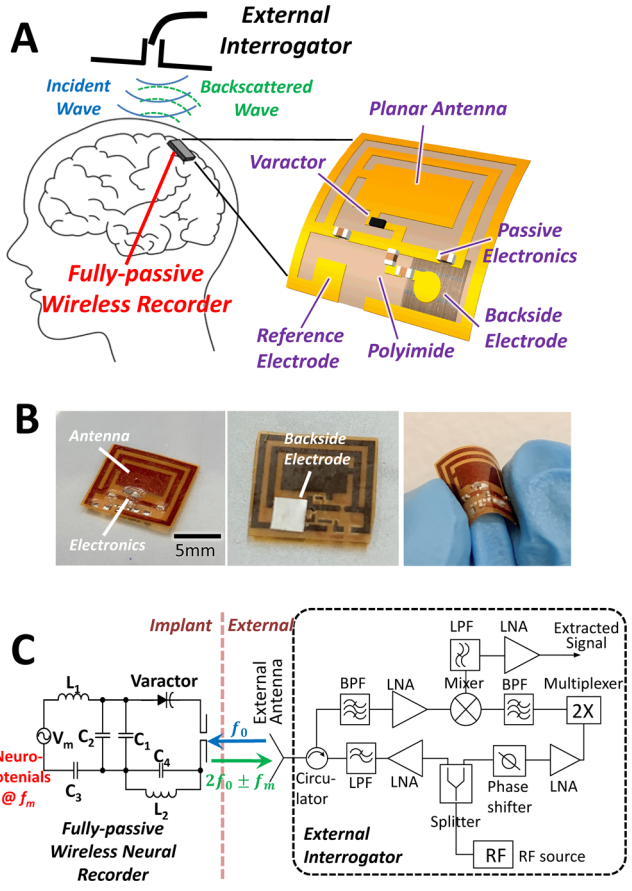

Figure 1. (A) Schematic of the fully passive wireless neural recorder. The flexible recorder is implanted to collect neuropotentials (f_m) through its backside electrode. The external interrogator generates and shines the RF carrier (f_0) onto the implanted neural recorder. The varactor diode mixes the RF carrier (f_0) with neuropotentials (f_m) to produce the third-order mixing product ($2f_0 \pm f_m$). This is subsequently backscattered to the external interrogator, where it undergoes a series of filtering and demodulating steps to extract the target neuropotentials. (B) Photographs of a fabricated fully passive wireless neural recorder prototype, highlighting its size and flexibility. (C) Left: the simplified equivalent circuit diagram of the recorder. Discrete passive electronic components include one varactor, two bypass capacitors C_1 and C_2, one RF choke inductor L_1, and one dc block capacitor C_3. V_m represents the target neuropotentials. Right: the detailed structure of the external interrogator for extracting the neuropotentials from the backscattered third-order mixing product ($2f_0 \pm f_m$).

antenna and circuit structure. Table 1 summarizes the characteristics of the targeted neuropotentials: SSEPs and IEDs.[32,46]

To maximize the transmission of the third-order mixing products, we designed a unique single-layer planar antenna (Figure S1) using the ANSYS HFSS (high frequency structure simulator) and ADS (advanced design system, Keysight). Figure 2A shows the 3D simulated model, depicting the fully passive wireless recorder inside a tissue-simulating phantom.

Table 1. Characteristics of Target Neuropotentials

neuropotentials	amplitude (μV)	duration (ms)
IED	100−300	50−500
SSEP	10−20	50−100

The phantom model contains five different layers: scalp, skull, dura, gray matter, and white matter, using thickness, permittivity, and conductivity parameters.[40,41] The neural recorder is placed between the dura and gray matter. An external dual-band antenna is also placed 8 mm above the scalp to establish the wireless link. The *S*-parameters from HFSS are incorporated into the ADS circuit model in Figure 2B. In the circuit model, the voltage source V_m represents the collected neuropotentials and V_0 is the radiated RF power. The impedance at the tissue−electrode interface, R_{in}, and major parasitic elements are included in the circuit model.

Capacitor C_4 and inductor L_2 in Figure 2B are used for circuit impedance tuning. Figure S2 shows the backscattered power of third-order mixing products ($2f_0 \pm f_m$) as a function of C_4 from 1 to 20 pF. The maximum power reaches when C_4 = 11 pF, corresponding to optimal impedance matching to the antenna. Figure 2C shows the simulated backscattered power at $2f_0 \pm f_m$ as a function of the neuropotential amplitude. We observe that the minimum detectable signal becomes approximately 60 μV_{pp} when P_0 = 12 dBm. This value matches well with our experimental data, given later. The neuropotentials are treated as a single-tone sinusoidal signal to demonstrate the operation of the system in simulation. In practice, neuropotentials occupy multiple frequency bands. To better represent the actual neuropotentials, Figure 2D shows the simulated output waveform of the external interrogator for different input signal shapes, including sine, square, and triangle. As depicted, the output closely follows the input, regardless of the signal waveform, proving the efficacy of the external interrogator. The square and triangle waveforms are approximated in the frequency domain using 50 harmonics, and the output waveforms are obtained via the harmonic balance simulator.

Verification of the Fully Passive Wireless Recorder in the Tissue-Simulating Phantom. The fully passive wireless neural recorder was first tested in a multilayer tissue-simulating phantom (Figure 3A), representing skin, bone, dura, gray matter, and white matter, following our previous recipes given in ref 41 and 47 (see Supporting Information, Table S2). The wireless recorder was placed between the dura and gray matter. Figure 3B illustrates the experimental setup. An arbitrary function generator (Agilent 33250A) supplied the emulated neuropotentials (20 μV_{pp}−2 mV_{pp}, 100 Hz−1 kHz) to the wireless neural recorder. A resistor (10 k−1000 kΩ) was connected in series with the recorder to account for the input impedance at the electrode−tissue interface.

The power of the third-order mixing product ($2f_0 \pm f_m$) at the external antenna was measured via a spectrum analyzer (Agilent 8563E). The external antenna was placed at three different heights (4, 8, and 13 mm) from above the skin phantom. The RF carrier power generated by the RF function generator was set at 12 dBm before amplification (26 dBm after amplified). We observe that the largest discrepancy between simulations and measurements is approximately 3 dB, likely because of fabrication errors and parasitics in the circuits. The measurement confirms the wireless neural recorder's capability to receive the RF carrier, modulate it with emulated neuropotentials, and backscatter the mixing product to the external interrogator.

Figure 3D compares the temporal waveforms of emulated neuropotential inputs and outputs from the external interrogator, including pulse, square, and sine waves of 2 mV_{pp} at 1000 Hz. In all the cases, the extracted output has close

DOI: 10.1021/acssensors.9b01491
ACS Sens. 2019, 4, 3175−3185

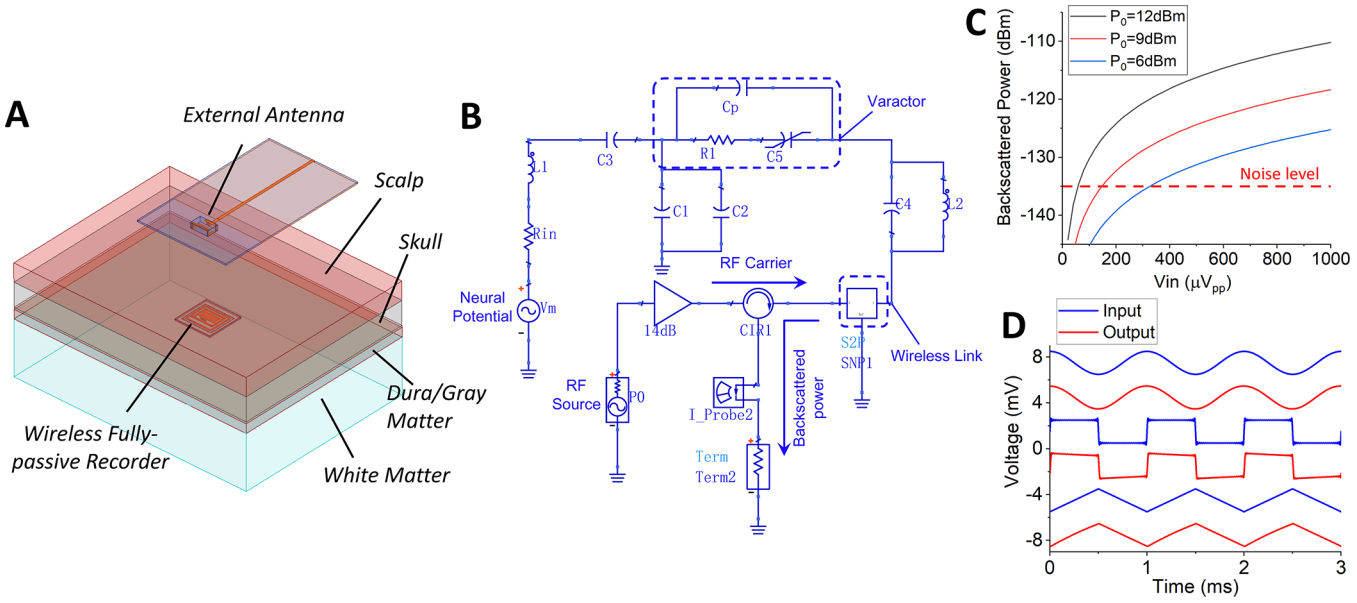

Figure 2. (A) 3D model of the fully passive wireless neural recorder inside a five-layer tissue phantom simulated using the HFSS. (B) Simplified ADS circuit model. The wireless link between the recorder and external antenna is modeled as a two port *S*-parameter network, extracted from HFSS simulation, and the backscattered power is obtained using the ADS harmonic balance simulator. (C) Backscattered power as a function of the neuropotential amplitude at three different input RF power (P_0) levels. The red dashed line represents the anticipated noise level of −135 dBm. (D) Temporal profiles of the output signals for sine, square, and triangle inputs, blue lines, (1 kHz, 2 mV_{pp}). The output, red color, refers to the signal extracted at the external interrogator.

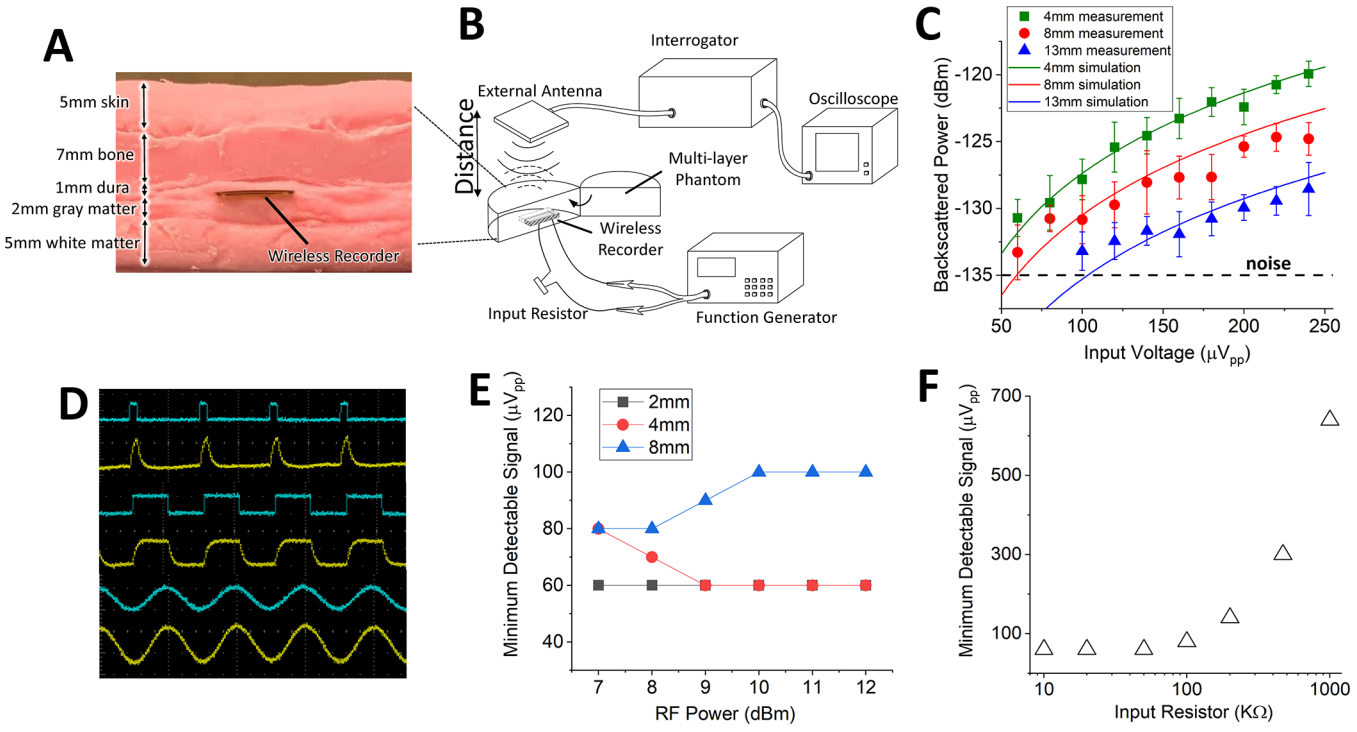

Figure 3. (A) Cross-section view of the fully passive wireless recorder placed inside the multilayer tissue-simulating phantom, representing the skin, bone, dura, gray matter, and white matter. The wireless implant was placed between the dura and gray matter. (B) Schematic of the experimental setup. The function generator inputted the emulated neuropotentials into the wireless neural recorder with a resistor simulating the impedance at the tissue−electrode interface. (C) Measured and simulated power of the backscattered third-order mixing product ($2f_0 \pm f_m$) as a function of the input signal amplitude, at 4, 8, and 13 mm distances. The black dashed line represents the averaged noise level (−135 dBm). (D) Transient waveform for the input and output signals. Blue: emulated neuropotentials (1 KHz, 2 mV_{pp}). Yellow: output signal extracted by the external interrogator. (E) Measured minimum detectable signal of the wireless recorder as a function of the input RF power. The input emulated potential was a 1 KHz square wave. (F) Measured minimum detectable signal as the input resistance. The minimum detectable signal remains less than 100 μV_{pp} when input impedance is less than 100 KΩ, while it significantly increases as the impedance increases up to 1 MΩ.

DOI: 10.1021/acssensors.9b01491
ACS Sens. 2019, 4, 3175−3185

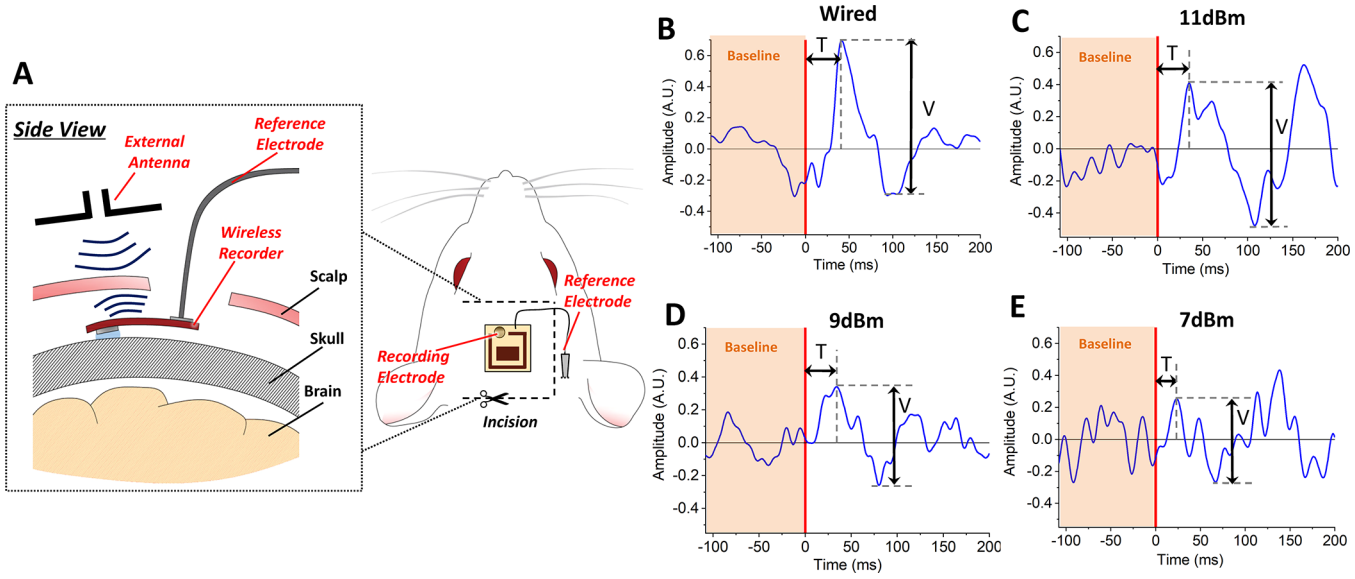

Figure 4. (A) Schematic of the experimental setup for in vivo SSEP recording. The fully passive wireless recorder was implanted subcutaneously to form the recording electrode on the rat skull. A stainless steel reference electrode was inserted subcutaneously over the contralateral (right) hemisphere of the rat. The wired SSEP recording electrode (not shown in plot) was placed at the very proximity of the location where wireless recording was performed for side-by-side comparison. Black dashed line represents the incision made on rat scalp. (B) Normalized in vivo SSEPs extracted from the wired recorder. (C–E) Normalized in vivo SSEPs extracted from the fully passive wireless recorder at an input RF power of 11 (C), 9 (D), and 7 dBm (E). The red lines at $t = 0$ ms mark the location of the stimulation event (3 mA at the rat's right hind limb). V and T denote the peak-to-peak amplitude of the evoked potentials and latency time from the positive peak to stimuli, respectively, as summarized in Table 2.

resemblance to the input signal demonstrating the effective operation of the wireless recorder for any arbitrary signal shape. Distortion of the output signal at the sharp edge is due to low-pass filtering. Figure 3E shows the detection limit of the wireless reorder when the external antenna is placed at 2, 4, and 8 mm from the skin. The minimum detectable signal denotes the minimum input peak-to-peak amplitude to produce 2 dB SNR at the output (see the Supporting Information for details). The minimum detectable signal improves as the RF power increases, as shown from the 2 and 4 mm data. The minimum detectable signal, on the other hand, actually suffers from the increased RF power, as shown in 8 mm data. This is because higher RF power also results in a rise in noise floor, leading to an unchanged or even decreased SNR. We recorded the minimum detectable signal as a function of the input resistance (Figure 3E). Because of the existence of noise, the minimum detectable signal of the wireless recorder increases from 60 to 640 μV_{pp} as the input resistance increases from 10 KΩ to 1 MΩ. We suspect that the noise mainly comes from the leakage current of our function generator and environment EM interference.

In Vivo Recording. The implanted recorder was first calibrated by ECG by concurrent recording of in vivo wired/wireless ECG signals (Figure S5). The close-up of the ECG waveforms reveals that the wireless ECG overlaps well with the wired ECG, exhibiting negligible delay, strongly supporting the fully passive wireless recorder being capable of capturing in vivo biopotentials under a fully implanted setting. The measured ECG also helps the alignment between the implanted wireless recorder and the external antenna.

In Vivo SSEP Acquisition. SSEPs extracted from wired and wireless recording are shown in Figure 4. The wired recorded SSEP signal (Figure 4B) depicts a distinct positive peak which is followed by a negative peak with slightly smaller amplitude, agreeing well with the previous published studies.[32] Similar positive and negative peaks were also observed in the wireless SSEP (Figure 4C–E). For better analysis, the two features, namely, the peak-to-peak amplitude (V) and latency from stimulus trigger (T), were extracted and compared as shown in Table 2.

The wireless SSEP amplitude shows an explicit drop as RF power decreases, which agrees well with our simulation (Figure 2) and phantom experiment (Figure 3). The wireless SSEP also marks consistent latency at 11 and 9 dBm, marking around 35 ms in both cases. At 7 dBm, the latency starts to show deviation, dropping from 35 to 24 ms. From observing the temporal waveform, it is clear that the wireless SSEP at 7 dBm suffers from a low SNR, which results in the positive and negative peaks becoming almost indistinguishable from the noise. For the wired SSEP, the latency is 41 ms, showing a 6 ms difference with that of the wireless SSEP (35 ms). Such discrepancy may come from our experimental procedures. Notably, because of the small area of S1HL, we were not able to perform wired and wireless recordings simultaneously. Instead, we first conducted wired recording, followed by wireless recording. This may result in the wired and wireless electrodes placed not exactly at the same places, leading to the difference in the recorded SSEP.

It should also be noted that the SSEP typically has a very small amplitude of less than 20 μV_{pp}, beyond the minimum detectable signal of the wireless recorder (60 μV_{pp} for this

Table 2. Wired/Wireless In vivo SSEP Recording Summary

recording	total number of trials	latency (T, ms)	amplitude (V, A.U.)
wired	2799	41	1
wireless @11 dBm	2999	35	0.89
wireless @9 dBm	2930	34	0.6
wireless @7 dBm	2908	24	0.55

DOI: 10.1021/acssensors.9b01491
ACS Sens. 2019, 4, 3175–3185

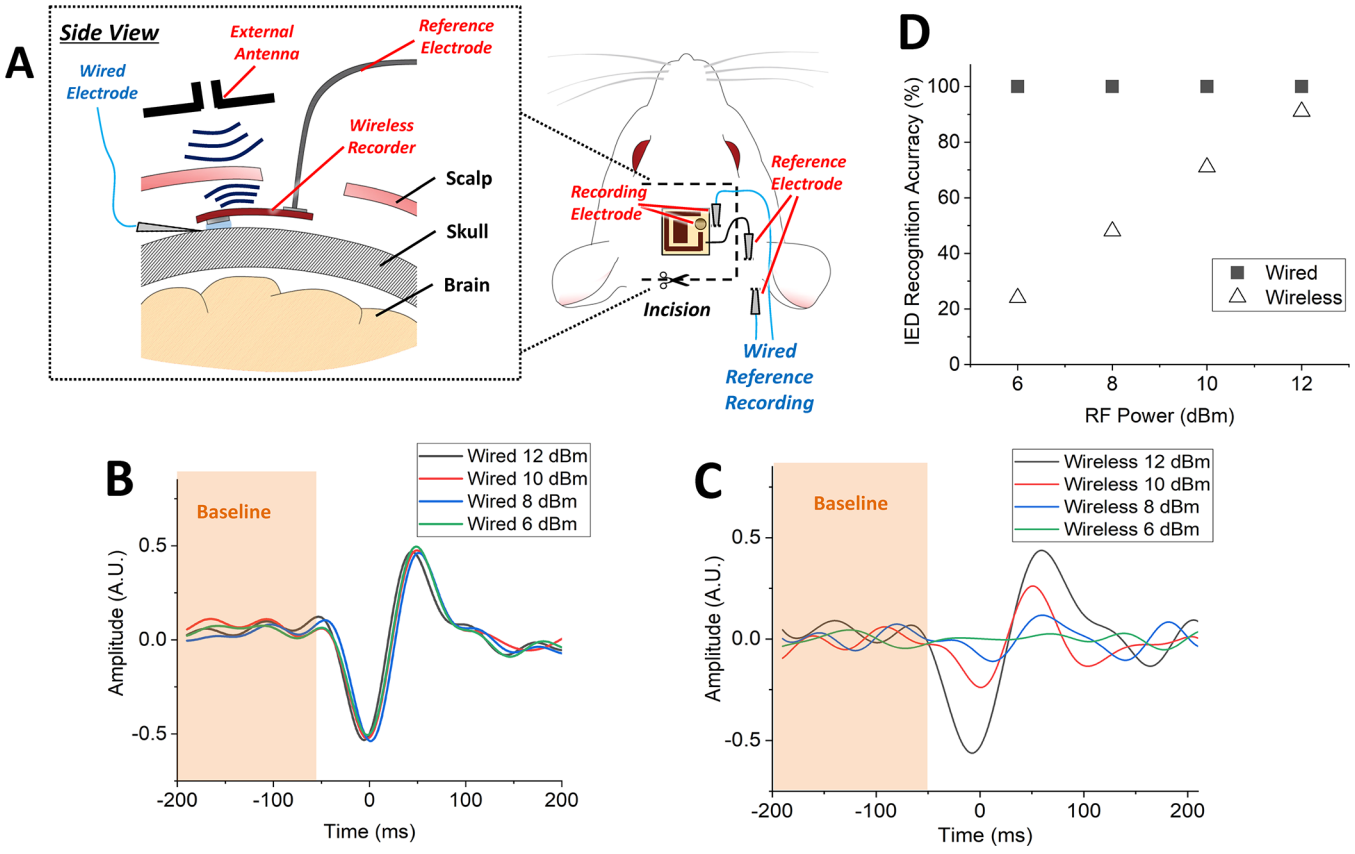

Figure 5. (A) Schematic of the experimental setup for in vivo IED recording. A wired recording electrode, connecting to AD Instrument Bio Amp, was placed right next to the wireless recorder with a distance of <2 mm for synchronized wired IED recording. The reference electrodes for the wired and wireless recording systems were inserted subcutaneously over the contralateral (right) hemisphere of the rat. (B,C) Normalized temporal waveforms of a single IED activity recorded by the wired (A) and wireless system (B) as a function of RF power. Amplitude of the wireless IEDs increase with RF power while that of the wired counterpart remains almost unchanged. (C) IED recognition accuracy using a machine learning algorithm. Labeled IED segments from wired and wireless data (12 dBm) were used to train the machine learning model. The accuracy marks 100% on the wired data, whereas it dramatically improves on the wireless data as RF power increases, agreeing well with the backscattering operation. Detailed IED recognition results are provided in Table 3.

experiment). We were able to obtain SSEPs by averaging thousands of stimulation trials (Table 2). Through averaging, the noise is canceled out and characteristic SSEP components are strengthened. The averaged wireless SSEP shows slightly larger fluctuation than the wired counterpart, and the amplitude and latency demonstrate strong coherence with wired data, which strongly validates our results.

In Vivo IED Acquisition. Figure 5A,B shows the normalized temporal waveform of the IED signal recorded by the wired system (AD Instrument Bio Amp) and the wireless recorder at various RF powers. The IED signal contains a rapid sharp negative component that lasts approximately 70 ms and is followed by a positive slow wave of 100 ms duration. This type of IED can be classified as interictal spikes, which are typical of cryptogenic and benign forms of epilepsy.[48] As shown in Figure 5A, the wired IED signals overlap well with each other, independent of RF power, indicating that the wired IED data remain unchanged when the RF power is varied. In contrast, the amplitude and signal quality of the wireless IED show strong dependence upon the RF power. At 12 dBm, the wireless IED shows closest resemblance to its wired counterpart. With the RF power decreasing, the amplitude of wireless IED notably drops, until it is completely indistinguishable at 6 dBm. The dependency of wireless signal quality upon the RF power agrees well with our simulations and in vitro validation results.

Table 3. Results of IED Recognition Using Machine Learning

		labeled	recognized labeled	accuracy (%)
12 dBm	wired	11	11	100
	wireless		10	91
10 dBm	wired	17	17	100
	wireless		12	71
8 dBm	wired	31	31	100
	wireless		15	48
6 dBm	wired	42	42	100
	wireless		10	24

The mean and standard deviation of seven independent IED signals recorded from wired and wireless recorders are shown in Figure S6. As expected, the wired recorder (AD Instrument Bio Amp) provides a high SNR. The wireless IED at 12 dBm marks an averaged peak-to-peak amplitude of 0.11 and an averaged standard deviation of 0.053, yielding an SNR of approximately −1.34 dB, suggesting that the IED signal is overshadowed by the noise. In comparison, the wired IED has an averaged peak-to-peak value of 0.362 and an averaged standard deviation of 0.018, which yields an SNR as high as

DOI: 10.1021/acssensors.9b01491
ACS Sens. 2019, 4, 3175−3185

Table 4. Specification of the Proposed Recorder in Comparison to Other State-of-the-Art Systems

	Borton[14]	Sodagar[15]	Muller[17]	Lee[21]	Seo[51]	this work
size	56 × 42 × 9 mm^3	15 × 14 mm^2	6.5 × 6.5 mm^2	19 × 19 × 30 mm^3	3 × 1 × 0.8 mm^3	9 × 8 × 0.3 mm^3
weight	44.5 g	275 mg		5.7 g		54 mg
no. of channel	100	64	64	32	1	1
power source	rechargeable battery	RF (70/200 M)	RF (300 M)	inductive (13.56 M)	ultrasound (1.85 M)	RF (2.32 G)
power consumption	90.6 mW	14.4 mW	225 μW	35 mW	0	0
minimum detectable signal	8.6 μV_{rms}	8 μV_{rms}	1.25 μV_{rms}	3 μV_{rms}	180 μV_{rms}	21.2 μV_{rms}
communication distance	1−3 m	10 mm	12.5 mm		8.8 mm	15−21 mm

8.53 dB. The signal collected by the wired electrode, recorded by our AD amplifier, marks a high SNR, and thus, the IED recognition may be a simple classification task of noise versus signal; however, the wirelessly recorded signal imposes a challenge for the recognition of IEDs. As the fully passive wireless recorder has little amplifying or digital coding capability, the wirelessly recorded IED signal is easily overshadowed by the noise and environmental artifacts. The low SNR of the wireless data results in a significant challenge to recognize IEDs using conventional signal processing methods, motivating us to adopt a machine learning-based pattern recognition algorithm to enable IED signal recognition. Furthermore, our concurrent wired/wireless signal acquisition allows the wired data to be used as a reference. In a practical setting, however, when only wireless recording is performed, no reference will be available. Therefore, the machine learning IED recognition technique adopted in this work is essential to analyze the wireless data.

For the training data set, we included both wired and wireless signal samples so that the machine learning model can recognize not only high SNR IED signals but also low SNR data. To ensure high recognition accuracy, only the best wireless IED signal, at 12 dBm, was used for training. Figure 5C illustrates the machine learning testing accuracy as a function of RF power. For the wired IED data, the testing accuracy remains at 100% under all the circumstances, which confirms the effectiveness of the developed machine learning model. For the wireless IED data, we observed that the testing accuracy improves as a function of RF power, from 24% at 6 dBm to as high as 91% at 12 dBm. This result suggests that although the wirelessly acquired temporal IED waveform is overshadowed by the noise and artifact, the machine learning algorithm can still recognize the low SNR IED signal from the unwanted noise, marking recognition accuracy as a function of the RF power. The increase of recognition accuracy with higher RF power also correlates well with our previous SSEP results. Detailed machine learning IED recognition results are provided in Table 3. It should be noted that the total number of IEDs recognized by the machine learning model, in both wired and wireless testing data sets, are significantly higher than what we labeled (see Supporting Information, Table S3). This outcome is possibly due to (1) the number of training data sets of labeled IED signal being limited and/or (2) the manual labeling being overconservative. As shown in Table S3, the rate of IED in our labeling is much smaller than that reported by other studies.[49,50] This may imply that many actual IEDs are missed in labeling.

Discussion. The in vivo recording of this work used both sequential (SSEP) and concurrent (IEDs) recording protocols. Specifically, the SSEP recordings focused on comparing averaged signals, indicating that spontaneous neural activity is averaged out and only a time-locked evoked signal remains. This requires using comparable electrode configuration, but not concurrent recording with both systems. It is known that the latency and amplitude of the processed evoked potential can vary with the animal, stimulation paradigm, and recording setup; however, keeping these factors consistent between our wireless and wired recordings will lead to common characteristic components (positive peak followed by a negative peak) of SSEPs. In this way, our wired recording data serve as a reference to evaluate the accuracy of our wireless system to reconstruct SSEP waveforms. In addition, a previous study[35] where SSEPs were recorded with a high-resolution EEG minicap shows how the extracted evoked potential may vary with distance from the corresponding somatosensory area. This further supports the use of sequential recordings, as it allowed us to place the recording electrode over the appropriate cortical area (according to ref 33, approximately 1.20 mm posterior to Bregma and 3 mm to the left of the midline) with the reference electrode in the same contralateral area and record in the same conditions with both systems.

On the other hand, IED recordings focused on spontaneously occurring characteristic components of epilepsy, implying that every recording trial would result in different IED occurrences, as they might be generated by different irritative brain zones. Therefore, spontaneous background activity cannot be averaged out, forcing us to record the IEDs concurrently with both systems. Trivially, the waveform of the IEDs will be different as recorded by both systems. Our focus was not in the exact waveform but in the capability to detect the IED peaks. The larger amplitude (hundreds of μV, peak-to-peak[36]) of the IEDs allowed the tolerance of the distance between the wireless and wired electrode to be considered negligible (<2 mm), supporting the similarity between the two signals despite the electrodes not being exactly identical.

It should be noted that the intended application for the presented wireless recorder is as a long-term implantable ECoG system. The tissue-emulating phantom (Figure 3) was designed to emulate this environment. However, the current dimension (9 mm × 8 mm) of the implant makes it very challenging to validate its functioning principles in vivo using a small animal such as rat, as this requires us to open a craniotomy (practically removing the entire skull and thus compromising physiology in this animal model). Our current in vivo experiments (Figures 4A, 5A) were used to validate the wireless signal transmission through the skin. The main objective of this work was to demonstrate the feasibility of neuropotential acquisition using the fully passive wireless system, via SSEPs & IEDs, as a function of signal power for a given wireless transmission. From both in vitro and in vivo data presented above, we conclude that the fully passive wireless system is very feasible through the skull−scalp interface.

Table 4 compares the specifications of our recorder with several other state-of-the-art neural recording systems. Several

DOI: 10.1021/acssensors.9b01491
ACS Sens. 2019, 4, 3175−3185

prior art features smaller footprint than ours, including the ultrasonic neural dust developed at Berkeley[51] ($3 \times 1 \times 0.8$ mm^3). The current footprint of our sensor may be significantly reduced by adopting advanced fabrication such as miro-3D printing as the antenna occupies a large footprint, and this remains as our future work.

Unlike inductive or ultrasonic coupling, our wireless fully passive recorder relies on the EM wave for the wireless telemetry. The EM wave shows significant adsorption in the body primarily dominated by dielectric and conductivity properties of the tissue. This directly impacts the amount of EM power to radiate from the external interrogator. In other words, we need to radiate higher power of the EM wave than inductive or ultrasonic waves at a given target power delivery. Our method, however, is not to power the implant but to collect the backscattered signal; thus, the amount of power being radiated can be drastically lowered. Nevertheless, the fundamental nature of tissue adsorption of the EM wave sometimes limits our applications.

The current wireless recorder still has many potential roadblocks impeding its practical implementation including its low SNR, susceptibility to environmental artifacts, and limited number of channels. Although the SNR may be improved by optimizing the antenna and circuit topology, the effect of artifact holds a significant challenge because of the lack of any digital coding capability on the recorder. Adding multichannel recording capability is another topic which requires further extensive research. Besides ECoG, the presented wireless recorder can also be used to collect other biopotentials such as in the heart (ECG) or muscle (EMG).[45] It is also possible to integrate both stimulating and recording functionalities into a single platform.[52] We will explore these challenges and opportunities toward our future research endeavors.

CONCLUSIONS

In this article, we reported a fully passive wireless neural recorder enabled by the RF backscattering method. The recorder features a small footprint of $9 \times 8 \times 0.3$ mm^3, high flexibility, and little power consumption because of the absence of any active or resistive components. We demonstrated the design and fabrication of the neural recorder and validated the recorder in vitro using a constructed multilayer tissue-simulating phantom and in vivo using an epileptic rat. Minimum detectable signal measurement in the phantom model confirmed a sensitivity of approximately 60 μV_{pp}. For in vivo validation, for the first time, the fully passive wireless recorder was implanted subcutaneously onto the rat skull to measure two types of neuropotentials, namely, SSEPs and IEDs. Wirelessly recorded SSEPs and IEDs not only showed close resemblance to the reference wired signals but also demonstrated consistent repeatable trends as a function of RF power. In addition, a machine learning-based IED recognition algorithm achieved 100 and 91% accuracy in wired and wireless data, respectively. These results strongly support the capability of the recorder to measure weak neuropotentials in a fully implanted setting, in a complete wireless and passive method. With further development and perfection, such device may have great potential and wide application in future wireless BMI systems.

ASSOCIATED CONTENT

Supporting Information

The Supporting Information is available free of charge on the ACS Publications website at DOI: 10.1021/acssensors.9b01491.

Design and fabrication of the fully passive wireless neural recorder, list of passive discrete electronic components on the wireless neural recorder, mixing behavior of the varactor diode, design and optimization of the circuitry, circuit model for simulation of external interrogator, determination of minimum detectable signal, calibration of the fully passive wireless neural reorder using in vivo ECG, mean and standard deviation of wired and wireless recorded IEDs, recipes for the five-layer tissue-emulating phantom, and comparison of the labeled IED and machine learning-recognized IED (PDF)

AUTHOR INFORMATION

Corresponding Author

*E-mail: Shiyi.liu.1@asu.edu.

ORCID

Shiyi Liu: 0000-0002-5653-4955

Notes

The authors declare no competing financial interest.

ACKNOWLEDGMENTS

This work was supported by the NSF award 1344928, "SCH: INT: Collaborative Research:Physiological Studies of Brain Signals using a Wireless Neuro-Sensing-Diagnoistic System" and NSF award 1734806, "NCS-FO: Collaborative Research: Fully-passive and wireless multi-channel neural recording for chronic in-vivo studies in animals".

REFERENCES

(1) Smith, S. J. M. EEG in the Diagnosis, Classification, and Management of Patients with Epilepsy. *J. Neurol., Neurosurg. Psychiatry* **2005**, *76*, ii2−ii7.

(2) Meierkord, H.; Dm, B. W.; Md, D. F.; Shorvon, S. The Clinical Features and Prognosis of Pseudoseizures Diagnosed Using Video-EEG Telemetry. *Neurology* **1991**, *41*, 1643.

(3) Menon, V.; Crottaz-Herbette, S. Combined EEG and FMRI Studies of Human Brain Function. *Int. Rev. Neurobiol.* **2005**, *66*, 291−321.

(4) Buzsáki, G.; Anastassiou, C. A.; Koch, C. The Origin of Extracellular Fields and Currents—EEG, ECoG, LFP and Spikes. *Nat. Rev. Neurosci.* **2012**, *13*, 407.

(5) Ramantani, G.; Maillard, L.; Koessler, L. Correlation of Invasive EEG and Scalp EEG. *Seizure* **2016**, *41*, 196−200.

(6) Khodagholy, D.; Gelinas, J. N.; Thesen, T.; Doyle, W.; Devinsky, O.; Malliaras, G. G.; Buzsáki, G. NeuroGrid: Recording Action Potentials from the Surface of the Brain. *Nat. Neurosci.* **2015**, *18*, 310.

(7) Wang, W.; Degenhart, A. D.; Collinger, J. L.; Vinjamuri, R.; Sudre, G. P.; Adelson, P. D.; Holder, D. L.; Leuthardt, E. C.; Moran, D. W.; Boninger, M. L. Human Motor Cortical Activity Recorded with Micro-ECoG Electrodes, during Individual Finger Movements. *2009 Annual International Conference of the IEEE Engineering in Medicine and Biology Society*; IEEE, 2009; pp 586−589.

(8) Rolston, J. D.; Englot, D. J.; Cornes, S.; Chang, E. F. Major and Minor Complications in Extraoperative Electrocorticography: A Review of a National Database. *Epilepsy Res.* **2016**, *122*, 26−29.

(9) Rolston, J. D.; Ouyang, D.; Englot, D. J.; Wang, D. D.; Chang, E. F. National Trends and Complication Rates for Invasive Extra-operative Electrocorticography in the USA. *J. Clin. Neurosci.* **2015**, *22*, 823−827.

DOI: 10.1021/acssensors.9b01491
ACS Sens. 2019, 4, 3175−3185

(10) Van Gompel, J. J.; Worrell, G. A.; Bell, M. L.; Patrick, T. A.; Cascino, G. D.; Raffel, C.; Marsh, W. R.; Meyer, F. B. Intracranial Electroencephalography with Subdural Grid Electrodes: Techniques, Complications, and Outcomes. *Neurosurgery* **2008**, *63*, 498−506.
(11) Vansteensel, M. J.; Pels, E. G. M.; Bleichner, M. G.; Branco, M. P.; Denison, T.; Freudenburg, Z. V.; Gosselaar, P.; Leinders, S.; Ottens, T. H.; Van Den Boom, M. A.; Van Rijen, P. C.; Aarnoutse, E. J.; Ramsey, N. F. Fully Implanted Brain−Computer Interface in a Locked-in Patient with ALS. *N. Engl. J. Med.* **2016**, *375*, 2060−2066.
(12) Schwarz, D. A.; Lebedev, M. A.; Hanson, T. L.; Dimitrov, D. F.; Lehew, G.; Meloy, J.; Rajangam, S.; Subramanian, V.; Ifft, P. J.; Li, Z.; Ramakrishnan, A.; Tate, A.; Zhuang, K. Z.; Nicolelis, M. A. L. Chronic, Wireless Recordings of Large-Scale Brain Activity in Freely Moving Rhesus Monkeys. *Nat. Methods* **2014**, *11*, 670.
(13) Anderson, G. S.; Harrison, R. R. Wireless Integrated Circuit for the Acquisition of Electrocorticogram Signals. *Proceedings of 2010 IEEE International Symposium on Circuits and Systems*; 2010; pp 2952−2955.
(14) Borton, D. A.; Yin, M.; Aceros, J.; Nurmikko, A. An Implantable Wireless Neural Interface for Recording Cortical Circuit Dynamics in Moving Primates. *J. Neural Eng.* **2013**, *10*, 026010.
(15) Sodagar, A. M.; Perlin, G. E.; Yao, Y.; Najafi, K.; Wise, K. D. An Implantable 64-Channel Wireless Microsystem for Single-Unit Neural Recording. *IEEE J. Solid State Circuits* **2009**, *44*, 2591−2604.
(16) Chestek, C. A.; Gilja, V.; Nuyujukian, P.; Kier, R. J.; Solzbacher, F.; Ryu, S. I.; Harrison, R. R.; Shenoy, K. V. HermesC: Low-Power Wireless Neural Recording System for Freely Moving Primates. *IEEE Trans. Neural Syst. Rehabil. Eng.* **2009**, *17*, 330−338.
(17) Muller, R.; Le, H.-P.; Li, W.; Ledochowitsch, P.; Gambini, S.; Bjorninen, T.; Koralek, A.; Carmena, J. M.; Maharbiz, M. M.; Alon, E.; et al. A Minimally Invasive 64-Channel Wireless #x03BC;ECoG Implant. *IEEE J. Solid State Circuits* **2015**, *50*, 344−359.
(18) Kipke, D. R.; Vetter, R. J.; Williams, J. C.; Hetke, J. F. Silicon-Substrate Intracortical Microelectrode Arrays for Long-Term Recording of Neuronal Spike Activity in Cerebral Cortex. *IEEE Trans. Neural Syst. Rehabil. Eng.* **2003**, *11*, 151−155.
(19) Tolstosheeva, E.; Hoeffmann, J.; Pistor, J.; Rotermund, D.; Schellenberg, T.; Boll, D.; Hertzberg, T.; Gordillo-Gonzalez, V.; Mandon, S.; Peters-Drolshagen, D. Towards a Wireless and Fully-Implantable ECoG System. *2013 Transducers & Eurosensors XXVII: The 17th International Conference on Solid-State Sensors, Actuators and Microsystems (TRANSDUCERS & EUROSENSORS XXVII)*; IEEE, 2013; pp 384−387.
(20) Lee, B.; Koripalli, M. K.; Jia, Y.; Acosta, J.; Sendi, M. S. E.; Choi, Y.; Ghovanloo, M. An Implantable Peripheral Nerve Recording and Stimulation System for Experiments on Freely Moving Animal Subjects. *Sci. Rep.* **2018**, *8*, 6115.
(21) Lee, B.; Jia, Y.; Mirbozorgi, S. A.; Connolly, M.; Tong, X.; Zeng, Z.; Mahmoudi, B.; Ghovanloo, M. An Inductively-Powered Wireless Neural Recording and Stimulation System for Freely-Behaving Animals. *IEEE Trans.Biomed.Circuits Syst.* **2019**, *13*, 413−424.
(22) Wolf, P. D.; Reichert, W. M. Thermal Considerations for the Design of an Implanted Cortical Brain−Machine Interface (BMI). *Indwelling Neural Implants: Strategies for Contending with the in Vivo Environment*; CRC Press, 2008, 33−38.
(23) Barrese, J. C.; Rao, N.; Paroo, K.; Triebwasser, C.; Vargas-Irwin, C.; Franquemont, L.; Donoghue, J. P. Failure Mode Analysis of Silicon-Based Intracortical Microelectrode Arrays in Non-Human Primates. *J. Neural Eng.* **2013**, *10*, 066014.
(24) Bjerknes, S.; Skogseid, I. M.; Sæhle, T.; Dietrichs, E.; Toft, M. Surgical Site Infections after Deep Brain Stimulation Surgery: Frequency, Characteristics and Management in a 10-Year Period. *PLoS One* **2014**, *9*, No. e105288.
(25) Schulman, J. H. The Feasible FES System: Battery Powered BION Stimulator. *Proc. IEEE* **2008**, *96*, 1226−1239.
(26) Lee, C. W. L.; Kiourti, A.; Chae, J.; Volakis, J. L. A High-Sensitivity Fully Passive Neurosensing System for Wireless Brain Signal Monitoring. *IEEE Trans. Microw. Theory Tech.* **2015**, *63*, 2060−2068.
(27) Marom, T.; Goldfarb, A.; Russo, E.; Roth, Y. Battery Ingestion in Children. *Int. J. Pediatr. Otorhinolaryngol.* **2010**, *74*, 849−854.
(28) Chae, M.; Liu, W.; Yang, Z.; Chen, T.; Kim, J.; Sivaprakasam, M.; Yuce, M. A. 128-Channel 6mw Wireless Neural Recording Ic with on-the-Fly Spike Sorting and Uwb Tansmitter. *2008 IEEE International Solid-State Circuits Conference-Digest of Technical Papers*; IEEE, 2008; pp 146−603.
(29) Neihart, N. M.; Harrison, R. R. Micropower Circuits for Bidirectional Wireless Telemetry in Neural Recording Applications. *IEEE Trans. Biomed. Eng.* **2005**, *52*, 1950−1959.
(30) Mestais, C. S.; Charvet, G.; Sauter-Starace, F.; Foerster, M.; Ratel, D.; Benabid, A. L. WIMAGINE: Wireless 64-Channel ECoG Recording Implant for Long Term Clinical Applications. *IEEE Trans. Neural Syst. Rehabil. Eng.* **2015**, *23*, 10−21.
(31) Schwerdt, H. N.; Xu, W.; Shekhar, S.; Abbaspour-Tamijani, A.; Towe, B. C.; Miranda, F. A.; Chae, J. A Fully-Passive Wireless Microsystem for Recording of Neuropotentials Using RF Backscattering Methods. *J. Microelectromech. Syst.* **2011**, *20*, 1119−1130.
(32) Moncion, C.; Balachandar, L.; Bojja-Venkatakrishnan, S.; Riera, J. J.; Volakis, J. L. Fully-Passive Wireless Implant for Neuropotential Acquisition: An In Vivo Validation. *IEEE J.Electromagn., RF and Microw. Med. Biol.* **2019**, *3*, 199.
(33) Paxinos, G.; Watson, C. *The Rat Brain in Stereotaxic Coordinates: Hard Cover Edition*; Elsevier, 2006.
(34) Camp, N. V.; Verhoye, M.; der Linden, A. V. Stimulation of the Rat Somatosensory Cortex at Different Frequencies and Pulse Widths. *NMR Biomed.* **2006**, *19*, 10−17.
(35) Valdés-Hernández, P. A.; Bae, J.; Song, Y.; Sumiyoshi, A.; Aubert-Vázquez, E.; Riera, J. J. Validating Non-Invasive EEG Source Imaging Using Optimal Electrode Configurations on a Representative Rat Head Model. *Brain Topogr.* **2019**, *32*, 599−624.
(36) Song, Y.; Sanganahalli, B. G.; Hyder, F.; Lin, W.-C.; Riera, J. J. Distributions of Irritative Zones Are Related to Individual Alterations of Resting-State Networks in Focal Epilepsy. *PLoS One* **2015**, *10*, No. e0134352.
(37) Deshmukh, A.; Leichner, J.; Bae, J.; Song, Y.; Valdés-Hernández, P. A.; Lin, W.-C.; Riera, J. J. Histological Characterization of the Irritative Zones in Focal Cortical Dysplasia Using a Preclinical Rat Model. *Front. Cell. Neurosci.* **2018**, *12*. DOI: 10.3389/fncel.2018.00052
(38) Dodge, S.; Karam, L. Understanding How Image Quality Affects Deep Neural Networks. *2016 Eighth International Conference on Quality of Multimedia Experience (QoMEX)*; IEEE, 2016; pp 1−6.
(39) Karahan, S.; Yildirum, M. K.; Kirtac, K.; Rende, F. S.; Butun, G.; Ekenel, H. K. How Image Degradations Affect Deep CNN-Based Face Recognition? *2016 International Conference of the Biometrics Special Interest Group (BIOSIG)*; IEEE, 2016; pp 1−5.
(40) Schwerdt, H. N.; Miranda, F. A.; Chae, J. A Fully Passive Wireless Backscattering Neurorecording Microsystem Embedded in Dispersive Human-Head Phantom Medium. *IEEE Electron Device Lett.* **2012**, *33*, 908−910.
(41) Schwerdt, H. N.; Miranda, F. A.; Chae, J. Analysis of Electromagnetic Fields Induced in Operation of a Wireless Fully Passive Backscattering Neurorecording Microsystem in Emulated Human Head Tissue. *IEEE Trans. Microw. Theory Tech.* **2013**, *61*, 2170−2176.
(42) Schwerdt, H. N.; Miranda, F. A.; Chae, J. Wireless Fully Passive Multichannel Recording of Neuropotentials Using Photo-Activated RF Backscattering Methods. *IEEE Trans. Microw. Theory Tech.* **2015**, *63*, 2965−2970.
(43) Kiourti, A.; Lee, C. W.; Chae, J.; Volakis, J. L. A Wireless Fully Passive Neural Recording Device for Unobtrusive Neuropotential Monitoring. *IEEE Trans. Biomed. Eng.* **2016**, *63*, 131−137.
(44) Lee, C. W.; Kiourti, A.; Volakis, J. L. Miniaturized Fully Passive Brain Implant for Wireless Neuropotential Acquisition. *IEEE Antennas Wirel. Propag. Lett.* **2017**, *16*, 645−648.

DOI: 10.1021/acssensors.9b01491
ACS Sens. 2019, 4, 3175−3185

(45) Liu, S.; Meng, X.; Zhang, J.; Chae, J. A Wireless Fully-Passive Acquisition of Biopotentials. *Biosens. Bioelectron.* **2019**, *139*, 111336.
(46) Ramantani, G.; Dümpelmann, M.; Koessler, L.; Brandt, A.; Cosandier-Rimélé, D.; Zentner, J.; Schulze-Bonhage, A.; Maillard, L. G. Simultaneous Subdural and Scalp EEG Correlates of Frontal Lobe Epileptic Sources. *Epilepsia* **2014**, *55*, 278−288.
(47) Ito, K.; Furuya, K.; Okano, Y.; Hamada, L. Development and Characteristics of a Biological Tissue-equivalent Phantom for Microwaves. *Electron. Commun. Jpn. Part I Commun.* **2001**, *84*, 67−77.
(48) Based, C. N. M. Interictal Epileptiform Discharges in Partial Epilepsy. *Jasper's Basic Mechanisms of the Epilepsies* **2012**, *80*, 213.
(49) Bortel, A.; Lévesque, M.; Biagini, G.; Gotman, J.; Avoli, M. Convulsive Status Epilepticus Duration as Determinant for Epileptogenesis and Interictal Discharge Generation in the Rat Limbic System. *Neurobiol. Dis.* **2010**, *40*, 478−489.
(50) Lévesque, M.; Behr, C.; Avoli, M. The Anti-Ictogenic Effects of Levetiracetam Are Mirrored by Interictal Spiking and High-Frequency Oscillation Changes in a Model of Temporal Lobe Epilepsy. *Seizure* **2015**, *25*, 18−25.
(51) Seo, D.; Neely, R. M.; Shen, K.; Singhal, U.; Alon, E.; Rabaey, J. M.; Carmena, J. M.; Maharbiz, M. M. Wireless Recording in the Peripheral Nervous System with Ultrasonic Neural Dust. *Neuron* **2016**, *91*, 529−539.
(52) Liu, S.; Navaei, A.; Meng, X.; Nikkhah, M.; Chae, J. Wireless Passive Stimulation of Engineered Cardiac Tissues. *ACS Sens.* **2017**, *2*, 1006−1012.

DOI: 10.1021/acssensors.9b01491
ACS Sens. 2019, 4, 3175−3185